POLYPUBLIE

Polarization-sensitive GeSn mid-infrared membrane photodetectors with integrated plasmonic metasurface. Supplément

Ziqiang Cai, Cédric Lemieux-Leduc, Mahmoud R. M. Atalla, Lu Luo, Gérard Tanguy Eric Gnato Daligou, Simone Assali, Oussama Moutanabbir

Document en libre accès dans PolyPublie
Open Access document in PolyPublie

Date	2026
Type	Article de revue/Article
Version	Matériel supplémentaire / Supplementary material
URL de PolyPublie PolyPublie URL	https://publications.polymtl.ca/74065/
Évaluation par les pairs Peer reviewed	Révisé par les pairs / Refereed
Conditions d'utilisation Terms of use	Creative Commons Attribution 4.0 International (CC BY)
Référence Citation	Cai, Z., Lemieux-Leduc, C., Atalla, M. R. M., Luo, L., Daligou, G. T. E. G., Assali, S., & Moutanabbir, O. (2026). Polarization-sensitive GeSn mid-infrared membrane photodetectors with integrated plasmonic metasurface. APL Photonics, 11(3), 036109 (9 pages). https://doi.org/10.1063/5.0313235

Publication officielle
Official publication

Titre de la revue Journal title	APL Photonics (vol. 11, no. 3)
Maison d'édition Publisher	AIP Publishing
URL officielle Official URL	https://doi.org/10.1063/5.0313235
Mention légale Legal notice	© 2026 Author(s). All article content, except where otherwise noted, is licensed under a Creative Commons Attribution (CC BY) license (https://creativecommons.org/licenses/by/4.0/).

Ce fichier a été téléchargé à partir de PolyPublie, le dépôt institutionnel de Polytechnique Montréal
This file has been downloaded from PolyPublie, the institutional repository of Polytechnique Montréal
https://publications.polymtl.ca

Supporting Information for
Polarization-sensitive GeSn Mid-Infrared Membrane Photodetectors with Integrated Plasmonic Metasurface

Ziqiang Cai, Cédric Lemieux-Leduc, Mahmoud R. M. Atalla, Luo Lu, Gérard Daligou, Simone Assali, and Oussama Moutanabbir[#]

Department of Engineering Physics, École Polytechnique de Montréal, Montréal, C.P. 6079, Succ. Centre-Ville, Montréal, Québec, Canada H3C 3A7

[#] Corresponding author. Email: oussama.moutanabbir@polymtl.ca

1. Refractive Index of GeSn

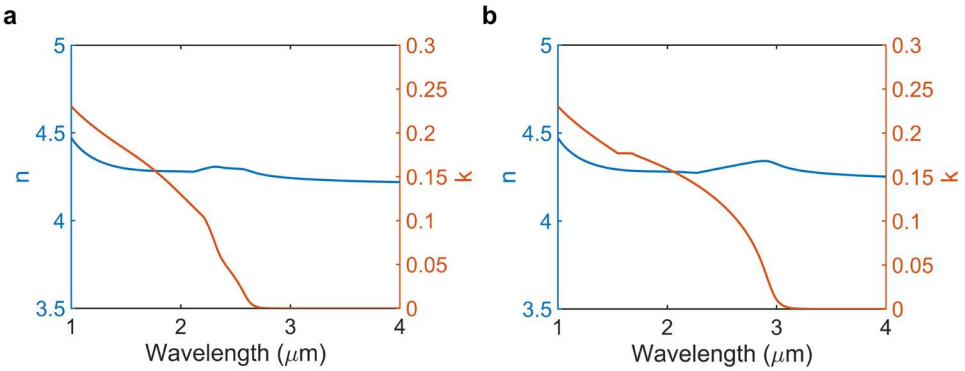


Figure S1. Real part n and imaginary part k of the refractive index of GeSn before (a) and after (b) releasing.

In the as-grown samples, the GeSn layer contains strain due to the lattice mismatch between layers during the chemical vapor deposition (CVD) growth. This strain is released after the underlying material is etched, creating a GeSn membrane. The resulting change in internal strain alters the band structure, leading to a substantial shift in the GeSn layer's cut-off wavelength. Accurate simulations require precise refractive index data for each material. However, the small size of the GeSn membrane makes it impossible to directly measure the refractive index via ellipsometry. Consequently, we can only measure the refractive index of

the as-grown GeSn sample, which we have done over a wavelength range from 0.21 μm to 2.5 μm. The refractive index for longer wavelengths must be calculated.

The refractive-index profiles of both the as-grown and released GeSn layers were computed independently within the same 8-band $k \cdot p$ framework, by first calculating the band structures and the absorption coefficients $\alpha(\lambda)$[1]. The model accounts for composition-dependent band parameters, strain, and material doping. For each case, the strain-dependent band structure was calculated using the 8-band $k \cdot p$ Hamiltonian, with strain impacts accounted via deformation-potential terms, modifying the band edges and valence-band splitting.[2, 3] All other parameters were kept identical. The wavelength-dependent refractive index, $\tilde{n}(\lambda) = n(\lambda) + i\kappa(\lambda)$, was derived directly from the absorption spectrum, and via the Kramers-Kronig relation [4]:

$$\kappa(\lambda) = \frac{4\pi}{\lambda}\alpha(\lambda), \qquad n(\lambda) = n(\infty) + \frac{2}{\pi}\mathcal{P}\int_0^{+\infty} \frac{\kappa(\lambda')d\lambda'}{\lambda'(1 - (\lambda'/\lambda)^2)}$$

where $\mathcal{P}$ denotes the Cauchy principal value and $n(\infty) = \sqrt{\varepsilon(\infty)}$ is the high-frequency refractive index associated with the electronic dielectric constant.

The composite refractive index profiles used in our simulations are shown in Figure S1. For both as-grown GeSn and released membrane, the profile is a combination of directly measured values at shorter wavelengths and calculated values at longer wavelengths. The redshift in the cutoff wavelength from 2.7 μm to 3.1 μm after strain release, as shown in Figure S1a and S1b, agrees well with the experiment data.

2. Measurement Setups

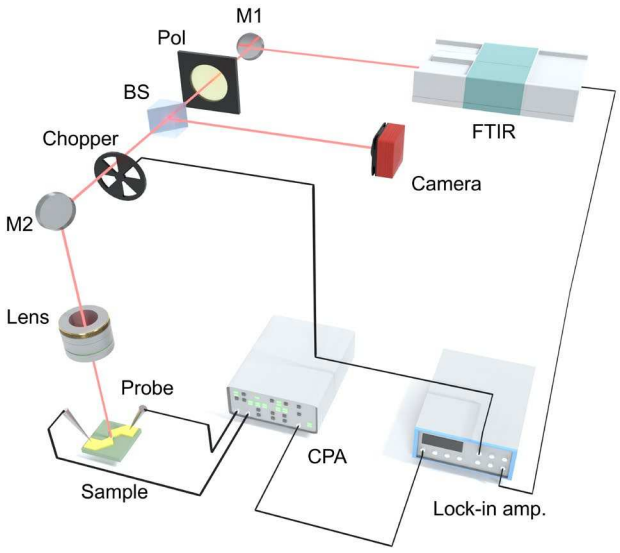


Figure S2. Schematic of the optical setup for the FTIR spectrum. 'M1' and 'M2' represent reflective mirrors. 'Pol' and 'BS' refer to polarizer and beam-splitter, respectively. CPA stands for current pre-amplifier. The red lines represent infrared light beams, and the black lines represent the electric wires.

The photodetector performance was characterized by the optical setup illustrated in Figure S2. Infrared light from a Fourier-transform infrared (FTIR) spectrometer (Bruker Vertex 70) was passed through a polarizer, a beam splitter, and a chopper before being focused onto the sample by a Cassegrain objective lens (Thorlabs LMM40X-UVV). The generated photocurrent was collected by electrical probes, then amplified sequentially by a current pre-amplifier (CPA) and a lock-in amplifier. The resulting signal was returned to the FTIR for processing. The use of a chopper, synchronized with the CPA and lock-in amplifier, significantly enhanced the signal-to-noise ratio. The FTIR spectrum was obtained by recording the signal while varying the optical path length difference in the interferometer, followed by a Fourier transformation to the recorded interferogram. Finally, the FTIR spectrum was normalized by the power spectrum of the light source of FTIR.

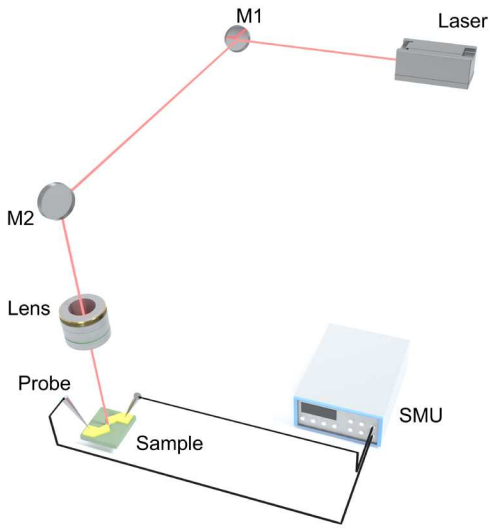


Figure S3. Schematic of the optical setup for the responsivity measurement. 'SMU' stands for source measure unit.

The absolute responsivity of the photodetector was measured using the setup depicted in Figure S3. The FTIR was replaced with a 1.55 μm infrared laser. The laser beam, with an optical power of 1.26 mW, was focused onto the GeSn membrane with a spot size of 7 μm in diameter. The photocurrent and dark current were measured using a source measure unit (SMU, Keithley 2470). To ensure the laser was optimally focused on the membrane, the sample stage was carefully adjusted until the photoresponse was maximized. Subsequently, current–voltage (I–V) characteristics were recorded with or without laser illumination to measure photo and dark currents. The photocurrent was calculated by subtracting the dark current from the total current measured under laser illumination.

3. Simulations of finite-sized GeSn membranes

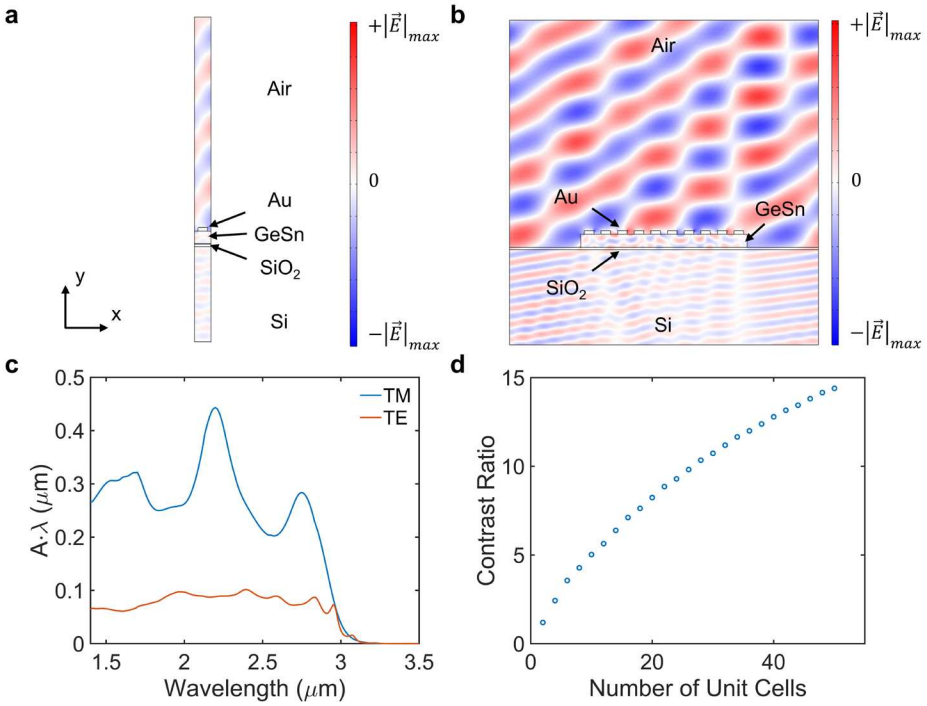


Figure S4. (a) Electric field distribution in one unit cell with periodic boundary conditions. (b) Electric field distribution for finite-sized membrane (10 unit cells) with perfect matching layer (PML) boundary conditions. (c) Corresponding responsivity spectra for finite-sized membrane. (d) Contrast ratios at 2.2 μm for finite-sized membranes with different number of unit cells. Incident wave is TM-polarized with a 30-degree angle of incidence.

Simulations of periodic metasurfaces typically employ periodic boundary conditions, which model an infinite array by calculating only a single unit cell. However, all metasurfaces are finite, leading to discrepancies between simulated and measured results. These discrepancies are particularly significant for smaller devices. The active area of our GeSn membrane photodetector is approximately 18 μm by 12 μm, which is not large relative to the operating wavelengths. To investigate the impact of finite size on device performance, we simulated the optical response of a finite-sized membrane (Figure S4b and S4c), which has 10 unit cells as an example. For comparison, Figure S4a present the simulated electric field distribution under periodic boundary conditions, and corresponding responsivity spectrum is shown in Figure 3e of the main text. Comparing these results, it reveals that the contrast ratio

is obviously lower for the finite-sized membrane. This explains why the measured contrast ratio is smaller than the initial simulation result. Furthermore, the electric field distribution in Figure S4b shows distinct diffraction patterns at the membrane edges compared to the center, illustrating the edge effect that alters the optical performance of device. We also simulated the contrast ratio for different membrane sizes, shown in Figure S4d. As the number of unit cells increases, the contrast ratio rises and will eventually saturate at the value of 31 for an infinitely large membrane. Note that we used 2D simulations for simplicity and didn't consider the finite dimension along the out-of-plane axis, which could further reduce the contrast ratio.

4. FTIR Spectra at Different Polarizer Angles

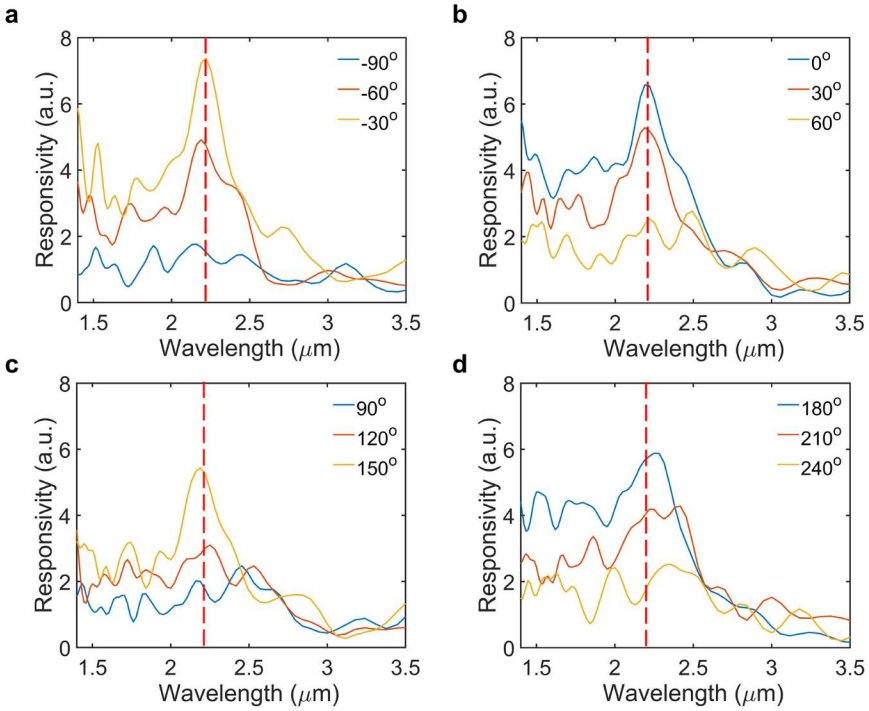


Figure S5. Responsivity spectra measured by FTIR with different polarizer angles: (a) -90°, -60°, -30°. (b) 0°, 30°, 60°. (c) 90°, 120°, 150°. (d) 180°, 210°, 240°. Red dashed lines indicate the wavelength of interest at 2.2 μm.

Figure S5 presents the responsivity spectra measured by FTIR with different polarizer angles. The data shown in Figure 3g is obtained by fixing the wavelength at 2.2 μm.

5. Measured Absolute Resoponsivities

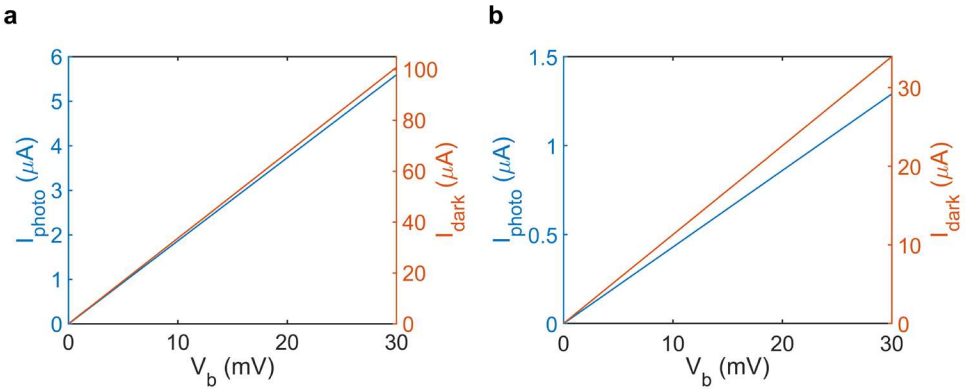


Figure S6. (a) Measured photocurrent (I_{photo}) and dark current (I_{dark}) of as-grown GeSn photodetector. (b) Measured I_{photo} and I_{dark} of GeSn membrane photodetector integrated with metasurface. The measurements are all taken at wavelength of 1.55 μm.

Figure S6 presents the measured I_{photo} and I_{dark} of the as-grown GeSn photodetector (a) and the GeSn membrane photodetector integrated with metasurface (b), using the measurement setup shown in Figure S3. Corresponding responsivities can be calculated through dividing I_{photo} by the optical power (1.26 mW) of incident laser beam. At a bias of 30 mV and wavelength of 1.55 μm, the as-grown device exhibits a responsivity of 4.43 mA/W, compared to 1.02 mA/W for the metasurface device. However, at a longer wavelength of 2.2 μm (also at 30 mV bias), the responsivities are 1.52 mA/W for the as-grown device and 2.01 mA/W for the metasurface device, deduced from FTIR spectra in Figure 3c and Figure 3f of the main text.

6. Tuning of Nanoribbon Width

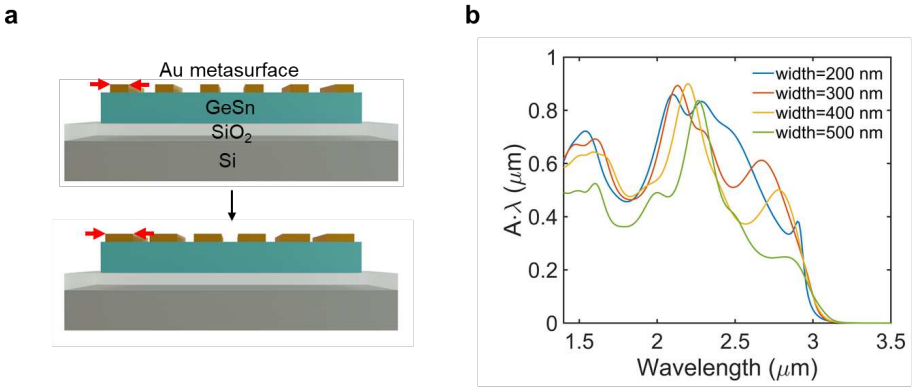


Figure S7. (a,b) Geometry and performance of metasurface-tuned photodetectors. (a) Schematics with varying grating widths. The period is kept constant. (b) Corresponding simulation results of responsivity spectra.

For metasurface gratings with nanostructure dimensions much smaller than the wavelength, the grating does not simply block incident light. Instead, it couples light into plasmonic resonances that modulate the local phase and amplitude of the optical field. To illustrate this, we simulated the responsivity spectrum as a function of grating width while keeping the period constant. As shown in Figure S7, increasing the grating width raises the filling ratio (width divided by period), yet the peak responsivity does not decrease monotonically. It reaches a maximum at a nanoribbon width of 400 nm. These results confirm that the interaction between light and the Au nanoribbons extends beyond simple optical blocking. On the contrary, light is coupled into plasmonic resonances, in which the coupling efficiency can be tuned by the grating geometry.

7. Influence of Cassegrain Lens

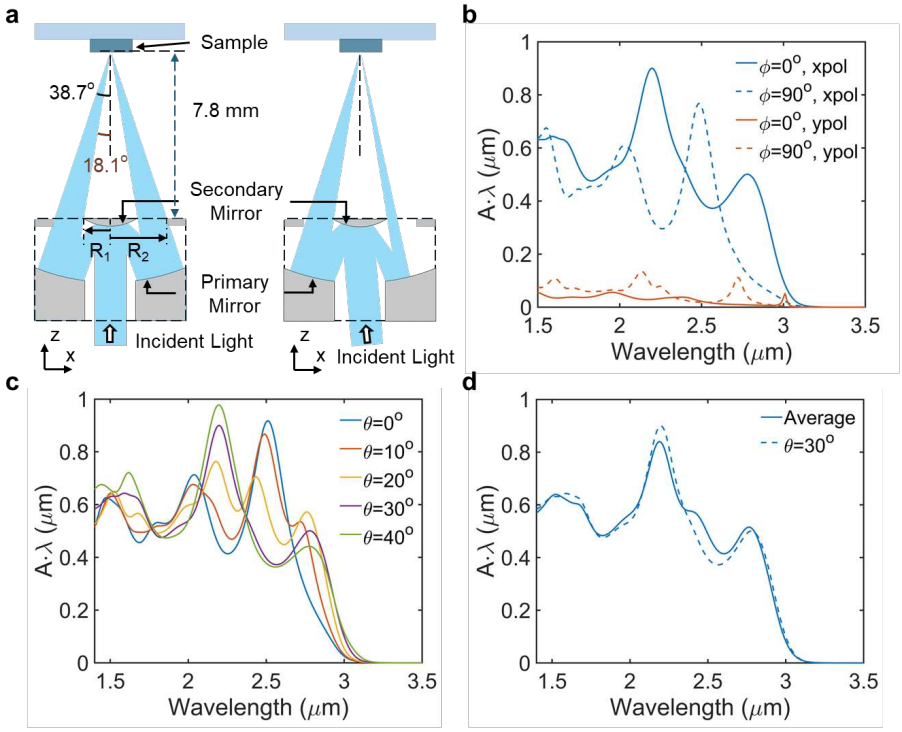


Figure S8. (a) Schematics of Cassegrain Lens with normal incidence (left) and tilted incidence (right). The xz-plane corresponds to azimuthal angle $\phi = 0^o$, and the yz-plane corresponds to $\phi = 90^o$. (b) Simulated responsivity spectra for different azimuthal angles and polarizations. (c) Simulated responsivity spectra for different incident angles (θ) and $\phi = 0^o$. (d) Spectrum from weighted average over all different θ (solid line) and the spectrum with $\theta = 30^o$ (dashed line).

The Cassegrain lens is commonly used in FTIR setups due to its ultra-broadband spectral coverage. However, its dual-mirror reflective design only allows light passing through with oblique incident angles, which complicates optical simulations, as shown in the left panel of Figure S8a. In our case, 3D simulation results show a clear difference between the responsivity spectrum at azimuthal angles $\phi = 0°$ and the spectrum at $\phi = 90°$ (Figure S8b), yet the measured spectrum closely matches the $\phi = 0°$ simulation rather than the average of these two. A plausible explanation is that the FTIR beam in our home-built setup is not perfectly aligned with the optical axis of the Cassegrain lens. This misalignment introduces a tilt in the beam entering the lens, breaking the azimuthal symmetry of the illumination and favoring rays with $\phi \approx 0°$, as illustrated in the right panel of Figure S8a. Although this asymmetry results from

imperfect alignment, the observed dominance of one azimuthal angle over the averaged response is beneficial for our target application. In typical infrared photodetection systems, light enters the device at near-normal incidence through a transmissive window or lens, rather than a reflective lens. Averaging the spectra from orthogonal azimuthal angles would obscure the distinct resonance features that exist at normal incidence. Therefore, the spectrum corresponding to a single azimuthal orientation is more representative of real-world operating conditions.

Apart from azimuthal variation, the responsivity spectrum also depends on the incident angle, as illustrated in Figure S8c. Because the incident optical power is not uniformly distributed across different angles, the measured spectrum represents a weighted average over the angular distribution: $\mathrm{S}(\lambda) = \int_{\theta=0}^{\theta=40^o} \mathrm{S_{xz}}(\lambda,\theta) \cdot P_{xz}(\theta) d\theta$, where $S_{xz}(\lambda,\theta)$ denotes the spectral response for light components in the xz-plane, and $P_{xz}(\theta)$ is the corresponding intensity fraction at angle θ.[4] The Cassegrain objective used in our experiment has a numerical aperture (NA) of 0.5, corresponding to a light ray angle of approximately 30^{o}. Consequently, most of the incident power is concentrated near 30^{o}, causing the weighted-average spectrum to closely match the spectrum at 30^{o} incidence, as shown in Figure S8d. For this reason, adopting a single incident angle of 30^{o} provides sufficient accuracy for our analysis.

References

1. Szmulowicz, F., Derivation of a General Expression for the Momentum Matrix-Elements within the Envelope-Function Approximation. *Phys. Rev. B* **1995,** *51* (3), 1613-1623.
2. Enders, P., Special-lines approximation to Brillouin zone integration. *Semicond. Sci. Technol.* **1996,** *11* (2), 187-189.
3. Liu, J.-m., *Photonic Devices*. Cambridge University Press: Cambridge, 2005.

4. Liang, Y.; Koshelev, K.; Zhang, F.; Lin, H.; Lin, S.; Wu, J.; Jia, B.; Kivshar, Y., Bound States in the Continuum in Anisotropic Plasmonic Metasurfaces. *Nano Lett.* **2020,** *20* (9), 6351-6356.